PCCP

Accepted Manuscript

ROYAL SOCIETY OF CHEMISTRY

www.rsc.org/pccp

Giant spin thermoelectric effects in all-carbon nanojunctions

X. F. Yang[1], H. L. Wang[1], Y. S. Chen[1], Y. W. Kuang[1],

X. K. Hong[1],* Y. S. Liu[1],† J. F. Feng[1], and X. F. Wang[2‡]

[1] *College of Physics and Engineering,*

Changshu Institute of Technology and Jiangsu Laboratory

of Advanced Functional materials, Changshu 215500, China

[2] *Department of physics, Soochow University, Suzhou 215006, China*

Abstract

We examine thermospin properties of an all-carbon nanojunction constructed by a graphene nanoflake (GNF) and zigzag-edged graphene nanoribbons (ZGNRs), bridged by the carbon atomic chains. The first-principles calculations show that the phonon thermal conductance is much weaker than the electron thermal conductance at the Fermi level, and even the former is a few percent of the latter in the low-temperature regime. Meantime, the carbon-based device possesses an excellent spin transport property at the Fermi level due to the appearance of a half-metallic property. And furthermore, the single-spin Seebeck coefficient has a larger value at the Fermi level. These facts ultimately result in a significant enhancement of spin thermoelectric figure of merit (FOM) Z_ST. By controlling the carbon-chain lengths and the temperature, the maximal value of Z_ST can reach 30. Moreover, we also find that the room temperature Z_ST displays an odd-even effect with the carbon-chain lengths, and it is always larger than the charge thermoelectric FOM Z_CT.

PACS numbers: 85.75.-d; 72.15.Jf; 85.80.-b

Keywords: All-carbon nanojunctions; Spin Seebeck effects; First-principles methods

1. INTRODUCTION

Spin Seebeck effect can implement the conversion from heat to spin current, then it is further transformed into the spin voltage by inverse spin Hall effects [1]. It provides a bran-new avenue to control the spin degree of freedom. In recent years, many theoretical and experimental works on spin Seebeck effect have been reported in various systems [2–17]. It is generally known that ideal thermospin materials need a high spin polarization of the linear conductance at the Fermi level to enhance spin transport and suppress charge transport. Meanwhile, it also should have lower thermal conductance to avoid the heat dissipation, and the stronger spin Seebeck effect is also a required condition. The spin thermoelectric performance of the material is thus expressed by the spin thermoelectric figure of merit (FOM) $Z_S T = S_S^2 G_S T/\kappa$, where S_S is the spin Seebeck coefficient, G_S is the spin conductance denoted by the difference between the linear conductance for different spin index, T is the temperature of materials, and κ is the thermal conductance including contributions from electrons and phonons.

Recently, carbon-based nanomaterials have been one of the most promising candidates for the miniaturization of electronic devices [18]. Especially, graphene, a two-dimensional (2D) single atomic layer of carbon, has inspired a large research interest since it was produced by mechanical exfoliations [19]. Due to its unique electronic properties, such as high electron mobility, long spin diffusion length, and strong stability resulting from the sp^2 hybridization, graphene has been regarded as an ideal material for future nanoelectronic devices. However, due to absence of the electronic band gap, graphene is very limited in electronic device applications. In addition, it also has an extremely high thermal conductivity [20]. Therefore, the thermoelectric performance is very weak. These facts indicate that the graphene is not good candidate for thermoelectric device applications. To improve its thermoelectric

performance, an effective avenue is to reduce dimensionality. For example, graphene can be tailored to one-dimensional graphene nanoribbons (GNRs) with armchair and zigzag edges. Molecular dynamics simulations show that the hydrogen-passivated GNRs are very stable at room temperature. All GNRs are semiconducting with direct band gaps, resulting in the high Seebeck coefficient near the Fermi level [21]. By optimizing doping levels, the charge thermoelectric FOM can reach 6 in the narrower armchair nanoribbons. However, this value is close to zero at the Fermi level due to the existence of the band gap. Recently, a new spin semiconducting property has been proposed in an all-carbon material, where an energy gap between spin-up and spin-down channels is found [22]. Further, a giant spin thermoelectric effect is shown in GNRs with sawtooth (ST) zigzag edges at room temperature [23]. We also note that Z_ST is very small at the Fermi level, which stems from an extremely low spin conductance.

In this paper, we propose a high-performance thermospin device based on an all-carbon nanojunction, in which a graphene nanoflake (GNF) is coupled to zigzag-edged graphene nanoribbons (ZGNRs) by the carbon atomic chains. It is found that the phonon thermal conductance is obviously weakened, and even it is a few percent of electron thermal conductance in the low-temperature regime. In addition, the spin-down Seebeck effect is obviously enhanced, meanwhile the device also shows a half-metallic property at the Fermi level. The maximal value of Z_ST can reach 30 by controlling the carbon-chain lengths and the temperature. Moveover, we also find that the room temperature Z_ST shows an odd-even oscillatory behavior with the carbon-chain lengths. Note, Z_ST is always larger than the charge thermoelectric FOM Z_CT. Our further analysis shows that the odd-even behavior is mainly determined by the spin-transport property at the Fermi level.

2. METHODS AND COMPUTATIONAL DETAILS

The all-carbon nanojunction is illustrated in Fig. 1(a), where one carbon atomic chain is bridged between the GNF and N-ZGNR electrodes. In this work, N=6 denotes the width of the ZGNRs (also see Fig. 1(a)). To assure the stability of the all-carbon nanojunction, all edge carbons are passivated by hydrogen. When a temperature difference ΔT between the left and right electrodes is provided, a spin-related voltage ΔV_σ can be produced. In the linear response region, the electric and heat currents in the spin channel σ are obtained by [24–28],

$$\Delta I_\sigma = \frac{e^2}{h} L_{0\sigma} \Delta V_\sigma + \frac{e}{h} L_{1\sigma} \frac{\Delta T}{T}, \tag{1}$$

and

$$\Delta J_\sigma = \frac{e}{h} L_{1\sigma} \Delta V_\sigma + \frac{1}{h} L_{2\sigma} \frac{\Delta T}{T}, \tag{2}$$

respectively. Here e is the electron charge and $L_{\nu\sigma}(E_F, T) = -\int d\epsilon \{\partial f(\epsilon, E_F, T)/\partial\epsilon\}(\epsilon - E_F)^\nu \tau_\sigma(\epsilon)(\nu = 0, 1, 2)$. $f(E, E_F, T)$ is the Fermi-Dirac distribution for the Fermi level E_F and the temperature T. $\tau_\sigma(\epsilon)$ is the spin-resolved transmission function at the electron energy ϵ, which is written by the Landauer-type equation as,

$$\tau_\sigma(\epsilon) = Tr[\mathbf{\Gamma}^L_\sigma(\epsilon) \boldsymbol{G}^r_\sigma(\epsilon) \mathbf{\Gamma}^{\boldsymbol{R}}_{\boldsymbol{\sigma}}(\epsilon) \boldsymbol{G}^a_\sigma(\epsilon)], \tag{3}$$

where $\boldsymbol{G}^{r(a)}_\sigma$ is the spin-dependent retarded (advanced) Green's function of the central scattering region and $\mathbf{\Gamma}^{L(R)}_\sigma$ the level broadening due to the coupling between the central scattering region and electrodes. $\tau_\sigma(\epsilon)$ can be obtained by the Atomistix ToolKit (ATK) package [29, 30]. Here the spin-dependent generalized gradient approximation with the the Perdew-Zunger (SLDA-PZ) exchange-correlation functional is employed. All carbon-based structures are built with vacuum space of width 15 Å. The energy cutoff of 150 Ry and a Monkhorst-Pack k-point mesh of $1 \times 1 \times 100$ for geometry optimization and transport calculations. During the optimization, all atoms in scattering region are relaxed

until the residual force on each atom is smaller than 0.02 eV/Å. With the aid of Eq. (1), we write the linear spin-dependent conductance at the Fermi level and temperature T as $G_\sigma = \frac{e^2}{h} L_{0\sigma}(E_F, T)$ for $\Delta T = 0$. Since the two spin channels related to spin-up and spin-down electrons are not mixed each other, we can introduce the spin-dependent Seebeck coefficient $S_\sigma = \lim_{\Delta T \to 0} \frac{\Delta V_\sigma}{\Delta T}|_{\Delta I_\sigma = 0}$ [31]. Using Eq. (1), we have [32, 33]

$$S_\sigma = -\frac{1}{eT} \frac{L_{1\sigma}(E_F, T)}{L_{0\sigma}(E_F, T)}, \tag{4}$$

The spin-dependent electron thermal conductance $\kappa_{el,\sigma}$ at the Fermi level E_F and temperature T is defined as $\kappa_{el,\sigma} = \lim_{\Delta T \to 0} \frac{\Delta J_\sigma}{\Delta T}$, which can be obtained by Eq. (2) and written as [33],

$$\kappa_{el,\sigma} = \frac{1}{h}[L_{1\sigma}(E_F, T) e S_\sigma + \frac{L_{2\sigma}(E_F, T)}{T}]. \tag{5}$$

The charge and spin Seebeck coefficients are then defined as $S_c = \frac{1}{2}(S_\uparrow + S_\downarrow)$ and $S_s = \frac{1}{2}(S_\uparrow - S_\downarrow)$, respectively. Finally, the charge and spin thermoelectric figure of merits are calculated by [28],

$$Z_c T = \frac{S_c^2 (G_\uparrow + G_\downarrow) T}{\kappa}, \tag{6}$$

and

$$Z_s T = \frac{S_s^2 (G_\uparrow - G_\downarrow) T}{\kappa}, \tag{7}$$

where $\kappa (= \kappa_{el,\uparrow} + \kappa_{el,\downarrow} + \kappa_{ph})$ is the total thermal conductance including contributions from electrons and phonons. The phonon thermal conductance κ_{ph} is obtained by [34],

$$\kappa_{ph} = \frac{\hbar^2}{2\pi} \int_0^\infty d\omega \tau_{ph}(\omega) \frac{\partial f_{ph}(\omega)}{\partial \omega} \tag{8}$$

where $\tau_{ph}(\omega)$ is the phonon transmission function, and ω is the frequency of phonons. $\tau_{ph}(\omega)$ can be evaluated by a similar Landauer-type equation as Eq. (3) after some substitutions [35]. A more concrete derivation for $\tau_{ph}(\omega)$ can be found in Ref. [36]. $f_{ph}(\omega) = \{e^{\hbar\omega/(k_B T)} - 1\}^{-1}$ in Eq. (8) denotes the Bose-Einstein distribution function of the heat carrier at the electrodes.

3. RESULTS AND DISCUSSION

Since the total energy of the all-carbon device in the ferromagnetic (FM) state is much lower than that of it in nonmagnetic and antiferromagnetic (AFM) state at room temperature, we here only consider the FM state, namely the spin in all atoms is initially arranged along the same direction. For the convenience of the subsequent discussion, we use the length of the carbon chains (C_n) to label different all-carbon devices. As representative examples, we present isosurface plots of the spin density ($\Delta\rho = \rho_\uparrow - \rho_\downarrow$) at the FM state for the C_5 and C_6 structures in Figs. 1(b) and 1(c), respectively. Similar to periodic ZGNRs, the spin in ZGNR parts mainly accumulates on edge carbon atoms. In addition, in comparison to the C_6 structure, we note that the C_5 structure shows the stronger magnetism on the carbon atomic chains and relatively weaker magnetism on the GNF. Magnetic moment distributions at carbon atomic chains for C_5 and C_6 structures are shown in Figs. 1(f) and 1(g), respectively. Obviously, for the C_6 structure, the net spin magnetism is much weaker. The main reason is that a complete alternation of single and triple bonds is generated in the C_6 structure, while this condition does not appear in the C_5 structure. The optimized bond lengths between the carbon atomic chain and ZGNRs, GNF and C-C bond lengths in carbon atomic chains are shown in Figs. 1(d) and (e). The results show that the C-C bond lengths between the end carbon atom and ZGNR or GNF are longer than the C-C bond lengths in carbon atomic chains. In addition, the carbon chain in the C_6 structure shows a polyyne-like bonding configuration [37–39].

The spin-resolved transmission spectra of the C_5 and C_6 structures versus electron energy are presented in Figs. 2(a) and (c), respectively. Interestingly, we find that the spin-down transmission in a wide energy region near the Fermi level is nearly suppressed to zero (e.g. $\tau_\downarrow = 2.4 \times 10^{-12}$ for the C_5 structure and $\tau_\downarrow = 1.3 \times 10^{-11}$ for the C_6 structure),

where the spin-down channels are completely blocked for transport. However, the spin-up channels are conductive, because $\tau_\uparrow$ at the Fermi level is about 0.4 for the C_5 and 0.3 for C_6 structures. This leads to a perfect half-metallic property at the Fermi level. In this case, the spin polarization of transport at the Fermi level, defined as $P = (\tau_\uparrow(\epsilon) - \tau_\downarrow(\epsilon))/(\tau_\uparrow(\epsilon) + \tau_\downarrow(\epsilon))|_{\epsilon=E_F} \times 100\%$, is close to its maximal value 100%. In order to further investigate the behind reasons, we plot the corresponding local density of state (LDOS) at the Fermi level in Figs. 2(b) and (d) for the C_5 and C_6 structures, respectively. The results show that the spin-up LDOS spreads the whole scattering region, while the spin-down LDOS only appears in ZGNR parts, and is completely in absence of the carbon atomic chains and GNF. Therefore, the spin-up electrons show the metallic property, while the spin-down electrons possess the semiconducting property. A perfect half-metallic property in the carbon-based device is achieved, and thus the spin linear conductance $(G_\uparrow - G_\downarrow)$ is enhanced to as large as the charge linear conductance $(G_\uparrow + G_\downarrow)$.

Compared with other electron energy points, the researchers are more concerned with the thermospin performance at the Fermi level. The spin-resolved Seebeck coefficient at the Fermi level as a function of temperature T is presented in Fig. 3(a) for the C_5 and C_6 structures. In the low-temperature regime (e.g. $0 < T \leq 50K$), the spin-dependent Seebeck coefficient S_σ is simplified as [33],

$$S_\sigma \simeq -\frac{\pi^2 k_B^2 T}{3e} \frac{\tau'_\sigma(\epsilon)}{\tau_\sigma(\epsilon)}|_{\epsilon=E_F}, \tag{9}$$

where the sign of S_σ is determined by the slope of τ_σ at the Fermi level. Therefore, we note that $S_\downarrow$ has a positive value for the C_5 structure due to $\tau'_\sigma(\epsilon)|_{\epsilon=E_F} < 0$ (see the inset in Fig. 2(a)) and a negative value for the C_6 structure due to $\tau'_\sigma(\epsilon)|_{\epsilon=E_F} > 0$ (see the inset in Fig. 2(c)) in the low-temperature regime. As the temperature is further increased, $S_\downarrow$ for the C_5 structure is enhanced to about 1800 $\mu V/K$ near 70K, and $S_\downarrow$ for the C_6 structure also

approaches 1500 $\mu V/K$ near 120K. Since an obvious enhancement of Seebeck coefficient is always attributed to the rapid increase or decrease of the corresponding transmission function, the behaviors of $S_\downarrow$ can be easily understood with the help of the transmission spectra presented in Fig. 2. For example, we clearly see that $\tau_\downarrow$ has a rapid increase at about 0.18 eV above the Fermi level for the C_5 and C_6 structures (see Figs. 2(a) and (c)). However, a smaller spin-down transmission peak at about 0.06 eV results in a slightly complicated behavior of $S_\downarrow$ with the temperature T for the C_6 structure. We even find that $S_\downarrow$ can also reach about 600 $\mu V/K$ at room temperature. In addition, one should note that $S_\uparrow$ for the C_5 and C_6 structures has a smaller value, which mainly originates from the metallic property of spin-up channels and a relatively flat structure for spin-up transmission function near the Fermi level. In Fig. 3(b), we plot the thermal conductance versus the temperature T for the C_5 and C_6 structures. To gain further insights into the dependence of electron thermal conductance on the temperatures, Eq. (5) is simplified as [41],

$$\kappa_{el,\sigma} \simeq \frac{2\pi^2 k_B^2 \tau_\sigma(E_F)}{3h} T. \tag{10}$$

The above equation clearly shows $\kappa_{el,\sigma}$ is proportional to the temperature T, and the analytical equation is in agreement with numerical results presented in Fig. 3(b). One should note that $\kappa_{el,\uparrow}$ has the main contributions to the electron thermal conductance $\kappa_{el}(=\kappa_{el,\uparrow}+\kappa_{el,\downarrow})$ due to $\tau_\downarrow(E_F) = 0.4$ and $\tau_\uparrow \simeq 0$. More interestingly, the phonon thermal conductance is always lower than the electron thermal conductance in the whole temperature region shown in Fig. 3(b). As T is further reduced, κ_{ph} is much more rapidly suppressed than κ_{el}. In the low-temperature regime, κ_{ph} is a few percent of κ_{el}. We also note that the periodic ZGNR has a phonon thermal conductance κ_{ph} of about 1.5 nW/K at the room temperature [40], while κ_{ph} in our device is decreased to about 0.017 nW/K. This leads to that $Z_S T$ and $Z_C T$ are insensitive to κ_{ph}. Finally, we note that the spin Seebeck coefficient S_S and charge

Seebeck coefficient S_C are obviously enhanced near 70K, and their magnitudes are nearly equal each other (see Fig. 3(c)). The maximal value of spin thermoelectric FOM Z_ST for the C_5 structure can reach 30 near 100K, and the maximal value of Z_ST for the C_6 structure can also approach 20 (see Fig. 3(d)). An even more intersecting is that Z_ST is larger than the charge thermoelectric FOM Z_CT near the room temperature (see the inset of Fig. 3(d)).

In order to further reveal the reasons why $S_\downarrow$ has a maximal value in the low-temperature regime, we refer to Eq. (4) and plot $L_{0\downarrow}$ and $L_{1\downarrow}$ as functions of the temperature T for the C_5 structure in Fig. 4. It is clearly shown that $L_{1\downarrow}$ has a negative value and keeps a linear relation with the temperature when $0 < T \leq 50K$, while $L_{0\downarrow}$ keeps unchanged (see Fig. 4(a)). As T is further increased, $L_{1\downarrow}$ is sharply enhanced near 70K. More importantly, $L_{0\downarrow}$ still keeps a constant until the temperature approaches 90K. In comparison to $L_{1\downarrow}$, such a delayed effect of $L_{0\downarrow}$ with respect to T leads to an obvious enhancement of $S_\downarrow$ near 70 K due to $|S_\downarrow| \propto |L_{1\downarrow}/L_{0\downarrow}|$. When $T \geq 90K$, $S_\downarrow$ is suppressed due to that $L_{0\downarrow}$ is obviously enhanced. As T is further increased, the rising trend of $L_{1\downarrow}$ is resemble with that of $L_{0\downarrow}$ (see Fig. 4(b)). Therefore, the change of $S_\downarrow$ with T is gradual near room temperature.

The dependence of thermospin effects of the all-carbon junctions on the length of carbon atomic chain at the Fermi level and room temperature is shown in Fig. 5. As the length increases, $S_\downarrow$ shows an odd-even oscillatory behavior, keeping a larger negative value. Meanwhile we find that $S_\uparrow$ has a smaller positive value, and it approaches a steady value as the length increases (see Fig. 5(a)). The corresponding spin-dependent linear conductance $G_\downarrow$ is plotted in Fig. 5(b). In comparison to $|S_\downarrow|$, $G_\downarrow$ has an inverse odd-even oscillatory behaviour as the length increases. We also find that $G_\uparrow$ and $S_\uparrow$ also exhibit an inverse odd-even oscillatory behaviour. When n is even (odd) number, $G_\uparrow$ has a lower (higher) value, while $G_\downarrow$ has a higher (lower) value. In Fig. 5(c), we plot the thermal conductance as a function of the length at room temperature. The electron thermal conductance is mainly determined

by the spin-up linear conductance due to $\kappa_{el} \propto (G_\uparrow + G_\downarrow)$. We also note that the phonon thermal conductance is insensitive to the carbon-chain length. Figure 5(d) demonstrates $Z_S T$ and $Z_C T$ have an odd-even behaviour as the length of the carbon atomic chain, and the odd-even behaviour is similar as $G_\uparrow$ (see Figs. 5(b) and (d))). In addition, $Z_S T$ is always larger than $Z_C T$ as the carbon-chain length increases.

The calculated transport properties of the all-carbon thermoelectric device (as an example, we take $C_n = 5$) versus the electron energy are presented in Fig. 6. The linear conductance G_σ has an obvious gap in the energy region of p-type doping ($\epsilon - E_F < 0$), and is obviously suppressed in the energy region. There is a sharp dip at about -0.8 eV for the spin-up linear conductance (marked by a black arrow) and about -0.6 eV for the spin-down linear conductance (marked by a red arrow). Here the linear conductance can be numerically calculated by $G_\sigma = \frac{e^2}{h} L_{0\sigma}$. As shown in Eq. (4), $L_{0\sigma}$ is the denominator of this equation. Therefore, S_σ can be strongly enhanced near these conductance dips. The maximum value of $|S_\sigma|$ can arrive at about 2000 $\mu V/K$ (see Fig. 6(b)). When T is 100K, the suppressed region of G_σ is broadened, and its value is further suppressed. The edge of the spin-down conductance is driven to close the Fermi level, resulting in a stronger spin-down Seebeck coefficient at the Fermi level. Meanwhile, the spin-up Seebeck coefficient at the Fermi level is near zero. Figure 6(c) shows k_{el} and k_{ph} versus the electron energy for $T = 300K$ and $T = 100K$. Due to $\kappa_{el} \propto G_\uparrow + G_\downarrow$, κ_{el} is also obviously suppressed in the negative energy region. We also note that κ_{ph} is suppressed as T is reduced (also see Fig. 3(b)). The corresponding thermoelectric FOM $Z_C T$ and $Z_S T$ are plotted in Fig. 6(d). We find that the peaks of $Z_S T$ and $Z_C T$ appear near the edges of the linear conductance. When T is tuned to 100K, the positions of right peaks are obviously shifted to close the Fermi level, and the heights of these peaks are enhanced. We thus have $Z_S T \simeq Z_C T \simeq 28$ at the Fermi level. In addition, one also should note that $Z_C T$ and $Z_S T$ are near zero in the energy

region [-0.8,-0.2] eV, which stems from $G_\uparrow \pm G_\downarrow \simeq 0$ and $Z_{C(S)}T \propto (G_\uparrow \pm G_\downarrow)$ in the energy region.

In summary, we have investigated the thermospin performance of an all-carbon nanojunction constructed by a graphene nanoflake (GNF) coupled to zigzag-edged graphene nanoribbons (ZGNRs) via the carbon chains. It is found that the phonon thermal conductance is much weaker than the corresponding electron thermal conductance. In the low-temperature regime, the phonon part is only a few percent of the electron part. Meantime, we find that the spin-down linear conductance at the Fermi level is obviously suppressed to close to zero, while the spin-up linear conductance has a larger value. As a result, the spin transport at the Fermi level is obviously enhanced. In addition, the spin-down Seebeck coefficient is obviously enhanced, and the spin-up Seebeck coefficient has a relatively small value. These facts ultimately result in a giant spin thermoelectric FOM at about 100K, and even it is larger than the corresponding charge thermoelectric FOM at room temperature.

ACKNOWLEDGMENTS

The authors thank the support of the National Natural Science Foundation of China (NSFC) (Grant Nos. 11247028, 61306122, 11347021, 61404012, 61274101, and 91121021). Y. S. Liu also thank the supports of the science and technology office project, the Six Talent Peaks Project, and Qing Lan project of Jiangsu Province.

* Electronic address: xuekh@mail.sitp.ac.cn

† Electronic address: ysliu@cslg.edu.cn

‡ Electronic address: xf_wang1969@yahoo.com

[1] K. Uchida, S. Takahashi, K. Harii, J. Ieda, W. Koshibae, K. Ando, S. Maekawa and E. Saitoh,

Nature, **455**, 778 (2008).

[2] H. Adachi, J. Ohe, S. Takahashi and S. Maekawa, Phys. Rev. B: Condens. Mater. Phys. , **83**, 094410 (2011).

[3] C. M. Jaworski, R. C. Myers, E. Johnston-Halperin and J. P. Heremans, Nature, **487**, 210 (2012).

[4] M. Weiler, M. Althammer, F. D. Czeschka, H. Huebl, M. S. Wagner, M. Opel, I. M. Imort, G. Reiss, A. Thomas, R. Gross and T. B. Goennenwein, Phys. Rev. Lett., 108, 106602 (2012).

[5] K. Uchida, T. Nonaka, T. Kikkawa, Y. Kajiwara and E. Saitoh, Phys. Rev. B: Condens. Matter Mater., **87**, 104412 (2013).

[6] M. G. Zeng, W. Huang and G. C. Liang, Nanoscale, 2013, 5, 200.

[7] M. Hatami, Gerrit E. W. Bauer, Q. F. Zhang, and P. J. Kelly, Phys. Rev. B **79**,174426 (2009).

[8] Y. S. Liu, X. F. Yang, F. Chi, M. S. Si, and Y. Guo, Appl. Phys. Lett. **101**, 213109 (2012).

[9] X. F. Yang, Y. S. Liu, X. Zhang, L. P. Zhou, X. F. Wang, F. Chi and J. F. Feng, Phys. Chem. Chem. Phys. , **16**, 11349 (2014).

[10] Y. S. Liu, X. Zhang, J. F. Feng and X. F. Wang, Appl. Phys. Lett. 104, 242412 (2014).

[11] X. F. Yang, Y. S. Liu, J. F. Feng and X. F. Wang, AIP Adv. , 4, 087116 (2014).

[12] M. X. Zhai, X. F. Wang, P. Vasilopoulos, Y. S. Liu, Y. J. Dong, L. P. Zhou, Y. J. Jiang, and W. L. You, Nanoscale, **6**, 11121 (2014).

[13] X. F. Yang, X. Zhang, X. K. Hong, Y. S. Liu, J. F. Feng, X. F. Wang and C. W. Zhang, RSC adv. 4, 48539 (2014).

[14] X. F. Yang, W. Q. Zhou, X. K. Hong, Y. S. Liu, X. F. Wang, and J. F. Feng, J. Chem. Phys. **142**, 024706 (2015).

[15] Y. S. Liu, W. Q. Zhou, J. F. Feng, and X. F. Wang, Chem. Phys. Lett. **625**, 14 (2015).

[16] Y. S. Liu, X. Zhang, X. F. Yang, X. K. Hong, J. F. Feng, M. S. Si and X. F. Wang, Phys.

Chem. Chem. Phys. **17**, 10462 (2015).

[17] X. F. Yang, H. L. Wang, X. K. Hong, Y. S. Liu, J. F. Feng, X. F. Wang, C. W. Zhang, F. Chi, and M. S. Si, Organic Electronics **24** 80 (2015).

[18] P. Avouris, Z. Chen and V. Perebeinos, Nat. Nanotechnol, **2**, 605 (2007).

[19] K. S. Novoselov, A. K. Geim, S. V. Morozov, D. Jiang, Y. Zhang, S. V. Dubonos, I. V. Grigorieva, and A. A. Firsov, Science **306**, 666 (2004).

[20] A. Balandin, S. Ghosh, W. Bao, I. Calizo, D. Teweldebrhan, F. Miao, and C. Lau, Nano lett. **8**, 902 (2008).

[21] H. Zheng, H. J. Liu, X. J. Tan, H. Y. Lv, L. Pan, J. Shi, and X. F. Tang, Appl. Phys. Lett. **100**,093104 (2012).

[22] Z. F. Wang, S. Jin, and F. Liu, Phys. Rev. Lett. **111**, 096803 (2013).

[23] X. B. Chen, Y. Z. Liu, B. L. Gu, W. H. Duan, and F. Liu, Phys. Rev. B **90**, 121403 (2014).

[24] G. D. Mahan, Many-Particle Physis (Plenum, New York, 2000)

[25] Y. Dubi and M. Di Ventra, Phys. Rev. B, **79**,081302 (2009).

[26] R. Świrkowicz, M. Wierzbicki, and J. Baranaś, Phys. Rev. B, **80**,195409 (2009).

[27] P. Trocha and J. Barnaś, Phys. Rev. B, **85**,085408 (2012).

[28] M. Wierzbicki, R. Świrkowicz, and J. Barnaś, Phys. Rev. B, **88**,235434 (2013).

[29] Atomistix ToolKit : Manual, Version 2008. 10.

[30] J. Taylor, H. Guo, and J. Wang, Phys. Rev. B 63, 245407 (2001).

[31] C. W. J. Beenakker and A. A. M. Staring Phys. Rev. B 46, 9667 (1992).

[32] U. Sivan and Y. Imry, Phys. Rev. B 33, 551 (1985).

[33] Y. S. Liu, F. Chi, X. F. Yang, and J. F. Feng, J. Appl. Phys. **109**, 053712 (2012).

[34] N. Mingo and D. A. Broido, Phys. Rev. Lett. **95**, 096105 (2005).

[35] K. K. Saha, T. Markussen, K. S. Thygesen, and B. K. Nikolić, Phys. Rev. B **84**,041412 (2011).

[36] X. L. Wei, G. C. Guo, T. Ouyang, and H. P. Xiao, J. Appl. Phys. **115**,154313 (2014).

[37] Z.H. Zhang, J. Zhang, G. Kwong, J. Li, Z. Fan, X. Deng, G. Tang, Sci. Rep. **3** 2575 (2013).

[38] Z. H. Zhang, C. Guo, D. J. Kwong, J. Li, X. Q. Deng, and Z. Q. Fan, Adv. Funct. Mater. **23**, 2765 (2013).

[39] Z.Q. Fan, Z.H. Zhang, F. Xie, X.Q.Deng, G. P.Tang, C.H.Yang, and K.Q. Chen, Phys. Lett. A, **378**, 1540 (2014).

[40] L. B. Liang, E. Cruz-Silva, E. Costa Girão, and V. Meunier, Phys. Rev. B, **86**, 115438 (2012).

[41] Y. S. Liu, Y. R. Chen, and Y. C. Chen, Asc Nano, **3**, 3497 (2009).

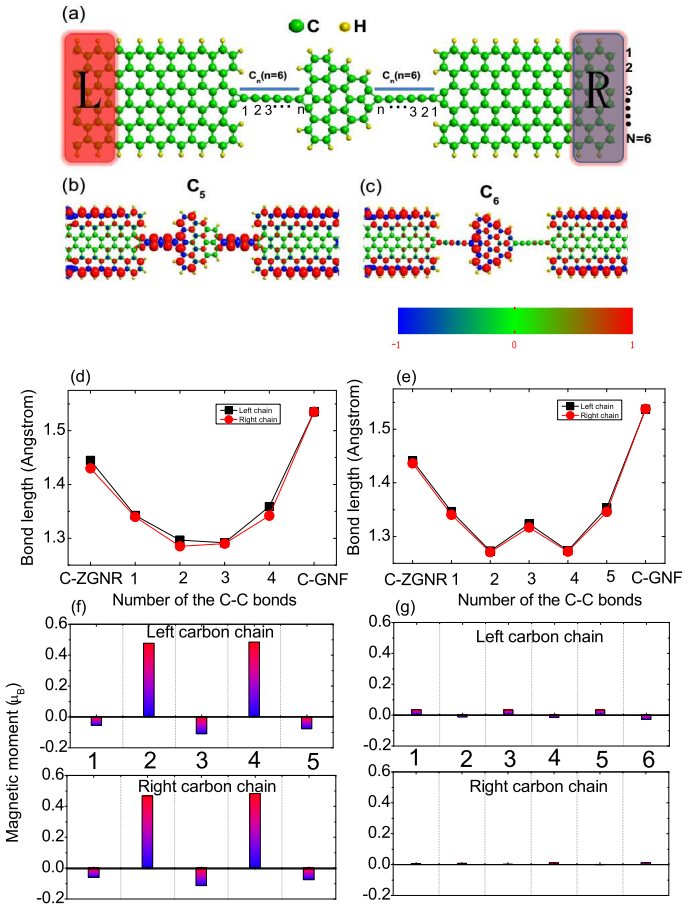

FIG. 1: (Color online) (a) Schematic view of the all-carbon nanojunction consisting of a graphene nanoflake coupled to zigzag-edged graphene nanoribbons via the carbon chains with different lengths. The symbol L and R represent the left and right electrodes, respectively. (b) and (c) Space distributions (top view) for the spin density ($\Delta\rho = \rho_\uparrow - \rho_\downarrow$) for the C_5 and C_6 structures, respectively. The isosurface value is 0.003 $e/\mathring{A}^3$. The red and blue colors mean the spin-up and spin-down components, respectively. (d) and (e) Bond lengths of the carbon chains for the C_5 and C_6 structures, respectively. (f) and (g) Magnetic moment distributions on carbon chains for the C_5 and C_6 structures.

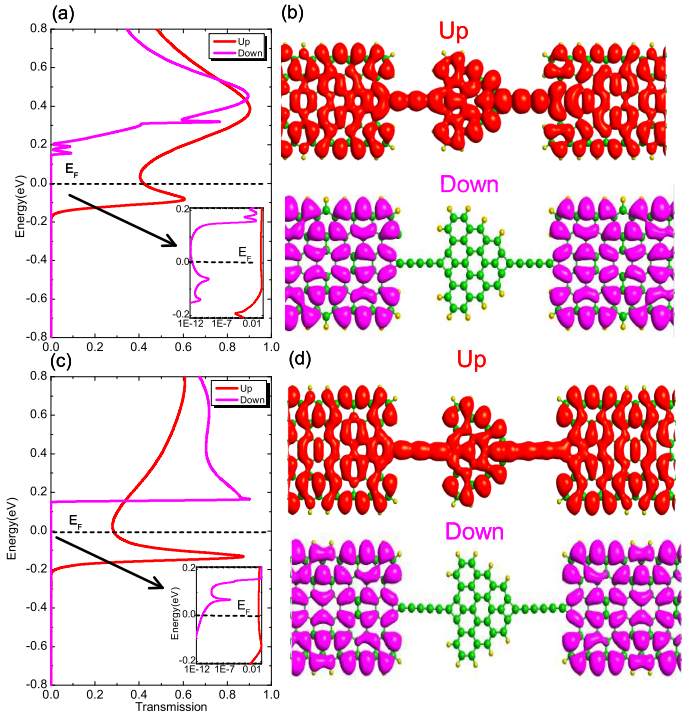

FIG. 2: (Color online) (a) Spin-dependent transmission spectrum for C_5 and its logarithm in the energy region [-0.2, 0.2] eV(inset). (b) Spin-dependent LDOS at the Fermi level. The isosurface value is 0.003 $e/\mathring{A}^3$. (c) Spin-dependent transmission spectrum for C_6 and its logarithm in the energy region [-0.2, 0.2] eV (inset). (d) Spin-dependent LDOS at the Fermi level.The isosurface value is 0.003 $e/\mathring{A}^3$. The Fermi level is fixed at zero energy point.

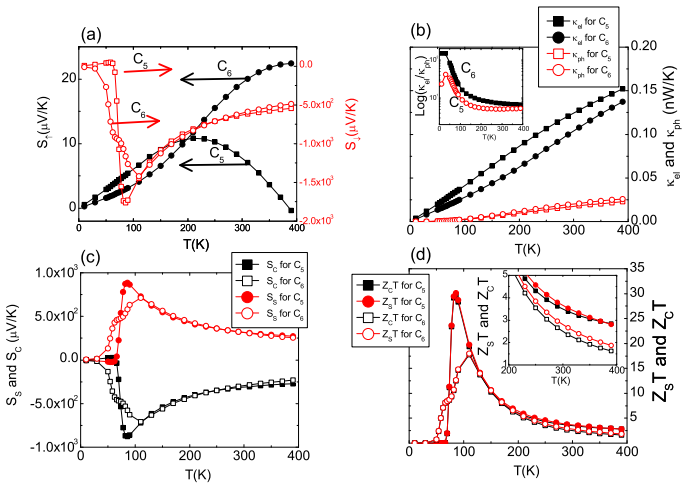

FIG. 3: (Color online) (a) Spin-dependent Seebeck coefficients, (b) phonon and electron thermal conductances, (c) spin and charge Seebeck coefficients, and (d) spin and charge thermoelectric FOMs as functions of the temperature T for the C_5 and C_6 structures.

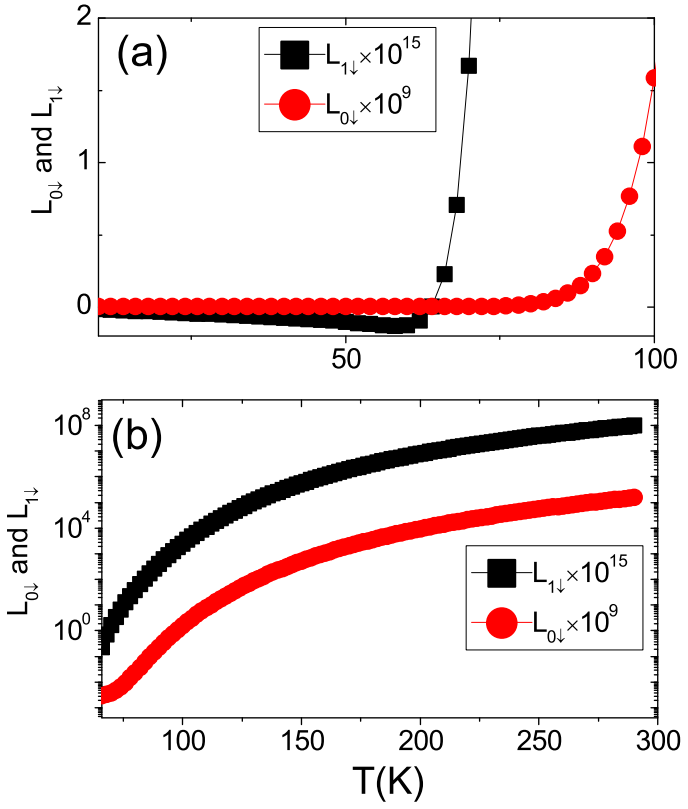

FIG. 4: (Color online) $L_{0\downarrow}$ and $L_{1\downarrow}$ as functions of T for the C_5 structure.

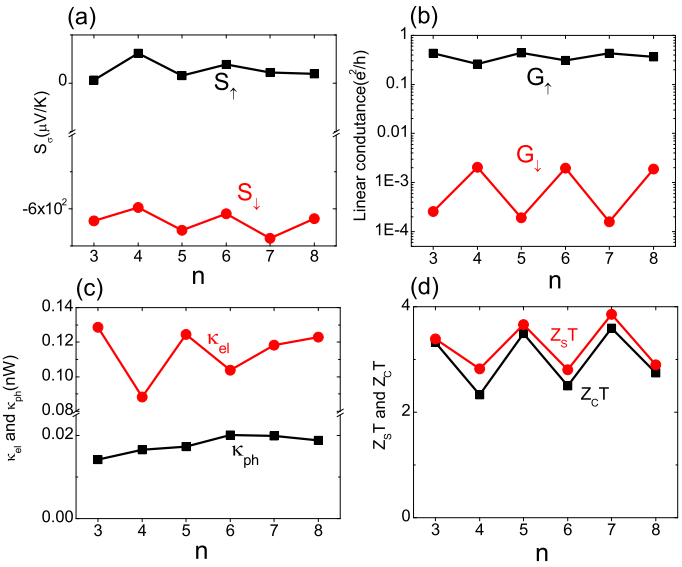

FIG. 5: (Color online) (a) Spin-dependent Seebeck coefficient S_σ, (b) spin-dependent linear conductance, (c) phonon and electron thermal conductance, and (d) spin and charge thermoelectric figure of merit as functions of the length of carbon atomic chains. The temperature T is 300 K.

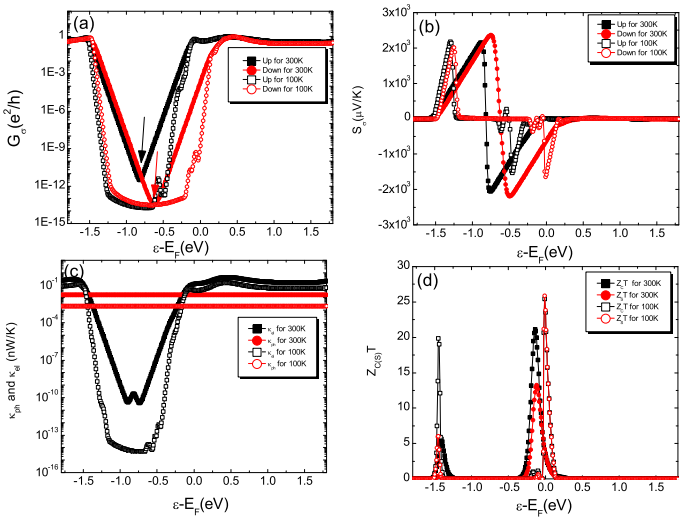

FIG. 6: (Color online) (a) Spin-dependent linear conductance, (b) spin-dependent Seebeck coefficient S_σ, (c) phonon and electron thermal conductances, and (d) spin and charge thermoelectric FOMs as functions of electron energy.